Inorganic Chemistry

pubs.acs.org/IC

Forum Article

Tunable Perovskite-Derived Bismuth Halides: $Cs_3Bi_2(Cl_{1-x}I_x)_9$

Emily E. Morgan, Lingling Mao,* Samuel M. L. Teicher, Guang Wu, and Ram Seshadri

Cite This: *Inorg. Chem.* 2020, 59, 3387−3393

Read Online

ACCESS | Metrics & More | Article Recommendations | Supporting Information

ABSTRACT: Bismuth-based perovskites are of interest as safer alternatives to lead-based optoelectronic materials. Prior studies have reported on the compounds $Cs_3Bi_2Cl_9$, $Cs_3Bi_2I_9$, and $Cs_3Bi_2Cl_3I_6$. Here we examine a range of compounds of the formula $Cs_3Bi_2(Cl_{1-x}I_x)_9$, where x takes values from 0.09 to 0.52. Powder and single-crystal X-ray diffraction were used to determine that all of these compounds adopt the layered vacancy-ordered perovskite structure observed for $Cs_3Bi_2Cl_3I_6$, which is also the high-temperature phase of $Cs_3Bi_2Cl_9$. We find that, even with very small iodine incorporation, the structure is switched to that of $Cs_3Bi_2Cl_3I_6$, with I atoms displaying a distinct preference for the capping sites on the BiX_6 octahedra. Optical absorption spectroscopy was employed to study the evolution of optical properties of these materials, and this is complemented by density functional theory electronic structure calculations. Three main absorption features were observed for these compounds, and with increasing x, the lowest-energy features are red-shifted.

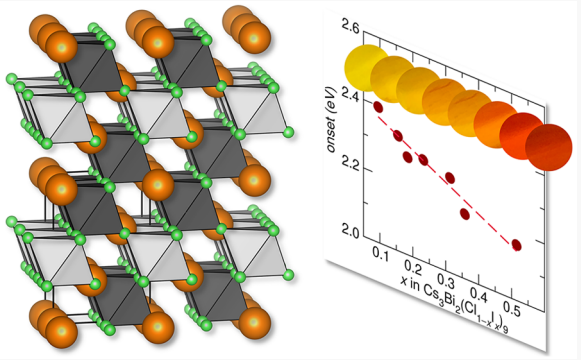

INTRODUCTION

In the past decade, significant improvements have been made in the efficiency of halide perovskite-based solar cells.[1] The most efficient devices have been made using lead-containing perovskites, which have the general chemical formula $APbX_3$, with efficiencies reaching 25.2% for perovskite cells and 28.0% for perovskite−silicon tandem cells.[2] Here, A denotes a monovalent cation, which is generally either a large inorganic cation, such as Cs^+, or a small organic cation, such as methylammonium or formamidinium, and X denotes a halide, usually Cl^-, Br^-, or I^-. Lead halide perovskites containing a mixture of different A site cations[3] and X site anions[4] have provided tunability of particular interest to researchers. Because these materials now display efficiencies comparable to those seen in commercially available silicon-based cells, it is likely that they will play a significant role in the future of solar energy.[1]

Despite the promise of lead halide perovskites, there is substantial concern as to whether they can be implemented on a large scale because of the toxicity associated with lead-based compounds. Although significant lead emissions are already associated with conventional industrial manufacturing and power generation technologies,[5] potentially disastrous levels of lead exposure could occur as a result of decomposition of lead perovskite solar cells.[6] While there may be methods to circumvent these issues, many researchers have sought lead-free perovskites that may be able to match the exciting optoelectronic properties associated with lead halide perovskites. Metals such as tin, germanium, antimony, and bismuth have been proposed as potential substitutes for lead; however, there have not been any reports of lead-free perovskites that have a comparable performance to the lead halide system.[7]

Among these metals, bismuth is viewed as one of the most promising alternatives to lead. Bismuth-based perovskites have attracted substantial attention because Bi^{3+} has the same electronic structure as Pb^{2+}, can form the perovskite structure, has low toxicity compared to that of lead, and is air-stable.[8] Accordingly, bismuth-based perovskites have been studied with a variety of combinations of A site cations and X site anions and in a range of forms, including thin films, nanocrystals, and bulk crystals.[9,10]

Previously, some of us have investigated bismuth-based materials such as BiI_3[11] and $A_3Bi_2I_9$ (A = K, Rb, Cs)[12] both experimentally and computationally, and concluded that these materials have properties that make them promising for photovoltaic applications. Furthermore, Park et al. proposed the compounds $Cs_3Bi_2I_9$, $MA_3Bi_2I_9$, and $MA_3Bi_2I_{9-x}Cl_x$ as photovoltaic materials with low toxicity, with $Cs_3Bi_2I_9$ exhibiting a power conversion efficiency of greater than 1%.[8] Subsequently, $Cs_3Bi_2I_9$ nanocrystals have been extensively studied for their photovoltaic properties,[13,14] and $MA_3Bi_2I_9$ thin films have achieved improved efficiencies of 3.17%.[15]

While these bismuth compounds are bulky 3D crystals, the connectivity of BiX_6 octahedra often yields an electronic

Special Issue: Bismuth - The Magic Element

Received: November 20, 2019
Published: February 4, 2020

https://dx.doi.org/10.1021/acs.inorgchem.9b03415
Inorg. Chem. 2020, 59, 3387−3393

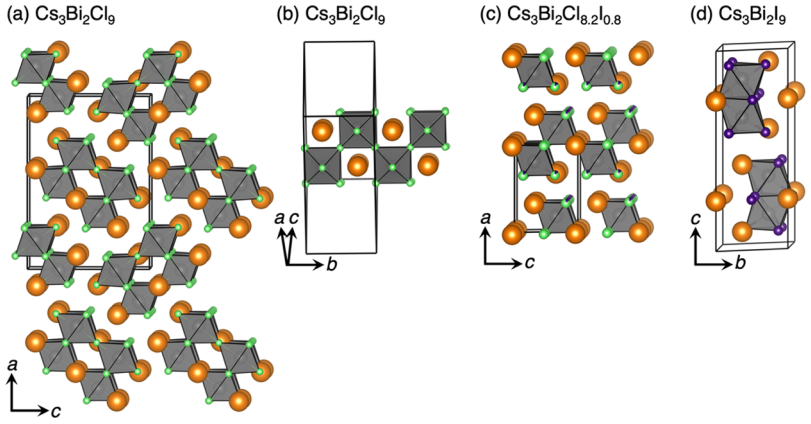

Figure 1. (a) 1D crystal structure of $Cs_3Bi_2Cl_9$ (*Pnma*, space group No. 62) viewed along the 1D chains of the $BiCl_6$ octahedra. (b) Same structure of $Cs_3Bi_2Cl_9$ emphasizing one of the chains of the $BiCl_6$ octahedra. (c) 2D vacancy-ordered perovskite structure of $Cs_3Bi_2Cl_{8.16}I_{0.84}$ [$P\bar{3}m1$ (No. 164)] viewed along the *b* axis, depicting the 2D sheets of the $BiCl_6$ octahedra. (d) 0D structure of $Cs_3Bi_2I_9$ [$P6_3/mmc$ (No. 194)] showing the condensed, face-shared double octahedra of $Bi_2I_9^{3-}$.

structure with effectively limited dimensionality. In their work, Xiao et al. demonstrated that in order for lead-free perovskites to match the efficiencies observed in the $APbX_3$ compounds, they must exhibit higher electronic dimensionality.[16] Thus, in order to improve the performance of materials such as $Cs_3Bi_2Cl_9$ and $Cs_3Bi_2I_9$, it is of interest to find ways to convert these structures, which feature 1D and 0D connectivity, respectively, to 2D connectivity. One example of this is the compound $Cs_3Bi_2I_6Cl_3$, which has a 2D-layered structure, an absorption edge of 2.07 eV, and a direct band gap.[17]

In this work, we expand the family of compounds with the formula $Cs_3Bi_2(Cl_{1-x}I_x)_9$, where x ranges from 0.09 to 0.52 through solution synthesis. The compounds were characterized by X-ray fluorescence (XRF) spectroscopy, single-crystal and powder X-ray diffraction (SCXRD and PXRD, respectively), UV−vis spectroscopy, and electronic structure calculations and compared to the end-member compounds. We find that adding small amounts of iodine to $Cs_3Bi_2Cl_9$ causes a large change in both the structure and electronic properties of the material and that adding successively greater amounts of iodine allows systematic tuning of the optical absorption edge within the visible region of the optical spectrum. Interestingly, the structures adopted by members of the solid solution described here are not stable structures of either of the end members, $Cs_3Bi_2Cl_9$ or $Cs_3Bi_2I_9$. Density functional theory (DFT)-based electronic structure calculations provide insights into the causes for dramatic changes in the optical absorption onset upon iodine substitution.

EXPERIMENTAL SECTION

All reagents were purchased from Sigma-Aldrich or Fisher Scientific and used without further purification or modification.

$Cs_3Bi_2Cl_9$ was prepared by adding 1 mmol of Bi_2O_3 to 4 cm^3 of HCl (37 wt % H_2O). The mixture was heated and stirred at 100 °C for 2 min to fully dissolve Bi_2O_3. A total of 3 mmol of CsCl was added to the solution, and the mixture was heated and stirred for an additional 5 min. After cooling, white crystals were isolated and dried by vacuum filtration.

$Cs_3Bi_2I_9$ was prepared by adding 1 mmol of Bi_2O_3 to a mixture of 4 mL of HI (57 wt % H_2O) and 0.15 cm^3 of H_3PO_2 (50 wt % H_2O). The mixture was heated and stirred at 100 °C for 2 min to fully dissolve Bi_2O_3. A total of 3 mmol of CsCl was added to the solution, and the mixture was heated and stirred for an additional 5 min. After cooling, dark-red crystals were isolated and dried by vacuum filtration.

$Cs_3Bi_2Cl_{9-x}I_x$ samples were prepared by first preparing mixtures containing various proportions of HCl (37 wt % H_2O) and HI (57 wt % H_2O) by adding volumes of HI varying from 0.05 to 0.50 to 4 cm^3 of HCl. A total of 1 mmol of Bi_2O_3 was added to each acid solution. The mixtures were heated and stirred at 100 °C for 2 min to fully dissolve Bi_2O_3. A total of 3 mmol of CsCl was added to each solution, and the mixture was heated and stirred for an additional 15 min. After cooling, crystals ranging in color from yellow to reddish-orange were isolated and dried by vacuum filtration.

PXRD measurements were performed on a Panalytical Empyrean powder diffractometer in reflection mode with a Cu Kα radiation source. Rietveld analysis was performed to estimate the lattice parameters using the *TOPAS* software package.[18] Single-crystal X-ray diffraction (SCXRD) data were collected for $Cs_3Bi_2Cl_9$ and one $Cs_3Bi_2Cl_{9-x}I_x$ sample on a Bruker KAPPA APEX II diffractometer with an APEX II CCD detector, a TRIUMPH monochromator, and a Mo Kα radiation source (λ = 0.71073 Å). The crystal structure was solved by direct methods and refined by full-matrix least squares on F^2 using the *OLEX2* program package.[19] Crystal structures were visualized using the *VESTA* software package.[20] XRF data were collected using a Rigaku ZSX Primus IV XRF spectrometer, which was used to determine the relative mass percentages of Cl and I present in each sample. The program used was set up to detect Cs, Bi, Cl, and I using the Cs Kα, Bi Lα, Cl Kα, and I Kα lines with a scanning time of 15 s and a fixed angle measurement time of 15 s for each element. Multiple measurements, each with a scan diameter of 0.5 mm, were made for each compound, and the results were averaged to determine the composition of each compound. Absorbance spectra were obtained by measuring the diffuse reflectance on a Shimadzu UV3600 UV−vis−near-IR spectrometer equipped with an integrating sphere. Reflectance was converted to absorbance using the Kubelka−Munk transformation.[21]

DFT calculations were performed in *VASP*, version 5.4.4,[22−24] using the PBE[25] and HSE06[26] functionals and projected-augmented-wave (PAW) pseudopotentials[27,28] with energy convergence of better than 10^{-6} eV. PAW potentials were selected based on the version 5.2 recommendations. We used structural parameters from $Cs_3Bi_2Cl_9$ SCXRD for the 0D-connectivity space group No. 62 structure. For the 2D-connectivity structures in space group No. 164, we performed calculations using the structure refined from SCXRD for $Cs_3Bi_2I_{0.8}Cl_{8.2}$ as well as using lattice parameters linearly interpolated between hypothetical 0% and 100% iodine incorporation structures based on the trends from PXRD Rietveld fits (Figure 3). We employed a plane-wave energy cutoff of 500 eV and used the automatic *k*-mesh generation scheme with the length parameter *l* set to 20 and 30 for PBE and HSE06 calculations, respectively (l = 30 corresponds to a *k*-mesh of 4 × 4 × 2 for the space group No. 62 structure and a mesh between 5 × 5 × 3 and 4 × 4 × 3 for the space

https://dx.doi.org/10.1021/acs.inorgchem.9b03415
Inorg. Chem. 2020, 59, 3387−3393

group No. 164 structure). Band structure calculations were performed using a density of 30 and 16 k points per branch for PBE and HSE06 calculations, respectively. Using these parameters, the band gaps appear to be converged much better than 0.1 eV in all cases. Crystal-orbital Hamilton bonding analysis was performed in *LOBSTER*.[29−32]

RESULTS AND DISCUSSION

Single crystals of $Cs_3Bi_2Cl_9$ and of a compound whose composition was established to be $Cs_3Bi_2Cl_{8.16}I_{0.84}$ were obtained directly from the reaction mixtures, and their structures as determined from SCXRD at room temperature are shown in Figure 1. The conditions for single-crystal data collection and select crystallographic parameters are summarized in Table 1. The structure of $Cs_3Bi_2Cl_9$ matched the reported structure that was found at temperatures of up to T = 646 K. The structure is orthorhombic in the *Pnma* space group and can be visualized as 1D chains of clusters of $BiCl_6$ octahedra (Figure 1a,b). While this structure has corner-connected $BiCl_6$ octahedra reminiscent of perovskite, the disposition of these octahedra makes it difficult to relate this structure to perovskite. One test of perovskite with no A-site vacancies is to check whether the A sites describe the topology of a simple cubic lattice. This appears not to be the case for $Cs_3Bi_2Cl_9$.

Table 1. SCXRD Refinement Data and Results for Two Compounds in the Series Whose Crystal Structures Are Depicted

empirical formula	$Cs_3Bi_2Cl_9$	$Cs_3Bi_2Cl_{8.16}I_{0.84}$
fw (g mol^{-1})	1135.74	1212.61
cryst habit, color	rods, colorless	hexagonal plates, yellow
cryst syst	orthorhombic	trigonal
space group	*Pnma* (No. 62)	$P\bar{3}m1$ (No. 164)
temperature (K)	300	299
wavelength (Å)	0.71073	0.71073
a (Å)	18.644(5)	7.7587(6)
b (Å)	7.6182(19)	7.7587(6)
c (Å)	13.186(4)	9.5183(8)
α (deg)	90	90
α (deg)	90	90
γ (deg)	90	120
volume (Å^3)	1872.8(8)	496.21(9)
density (calcd) (g cm^{-3})	4.028	4.058
θ range (deg)	3.276−28.327	2.140−30.550
completeness to θ = 25.242° (%)	99.5	100
reflns collected	8746	3782
data/restraints/param	2497/0/76	616/0/20
GOF	1.100	1.097
final R indices [$I > 2\sigma(I)$]	R_{obs} = 0.0319	R_{obs} = 0.0261
	wR_{obs} = 0.0658	wR_{obs} = 0.0678

The compound $Cs_3Bi_2Cl_{8.16}I_{0.84}$ crystallizes in the trigonal space group $P\bar{3}m1$ and adopts a structure that can be described by an ordered vacancy (□) on the perovskite $A_3B_2\square X_9$, which results in layers of vacancies separated by double layers of BiX_6 octahedra. The structure is very similar to that of β-$Cs_3Bi_2Cl_9$ but with a unit cell that is 3.8% smaller than what is reported, potentially because of thermal expansion of the structure of β-$Cs_3Bi_2Cl_9$, as reported at 723 K.[33] In this structure, the BiX_6 octahedra are corner-sharing and form corrugated 2D layers (Figure 1c). In their characterization of the structure of $Cs_3Bi_2I_6Cl_3$, which has a similar structure, McCall et al. found that the I atoms preferred to occupy the capping positions on the octahedra in the structure, while the Cl atoms occupied the bridging positions between the octahedra.[17] In the refinement of the structure presented here for $Cs_3Bi_2Cl_{8.16}I_{0.84}$, we observed a similar tendency, with corner-sharing sites between octahedra occupied exclusively by Cl and a mixture of I and Cl atoms in the other sites. This site preference may provide the previously mentioned driving force for the incorporation of iodine into the structure because the structure tries to maximize the number of I atoms in the capping sites. The origin of this site preference is revisited in the discussion of the electronic structure.

The broad family of $A_3B_2\square X_9$ structures have been previously described[34] as adopting 0D, 1D, and 2D variants, based on the order−disorder framework developed by Dornberger-Schiff and Grenn-Niemann.[35] The 2D structures described here are also adopted by $Cs_3Sb_2I_9$[36] and $Rb_3Bi_2I_9$.[12]

For completion, Figure 1d displays the stable crystal structure of $Cs_3Bi_2I_9$, which is again not perovskite-derived because the BiI_6 form has face-sharing pairs.

The compositions of the different $Cs_3Bi_2Cl_{9-x}I_x$ compounds were determined using XRF, and the results are displayed in Figure 2. As expected, it was observed that the mass percentages of Cl and I vary linearly with the percentage of HI in the reaction mixture. Additionally, it should be noted that in a plot of I occupancy versus percent of HI in the reaction, the slope of the linear fit is close to 6% I/% HI, demonstrating that the occupancy of the X sites is not the same as the ratio of I/Cl in the reaction mixture. For example, when the reaction mixture contained 7.27% HI, the product had an I occupancy of 52%. It is clear from these results that there is a large driving force for the incorporation of iodine into the structure.

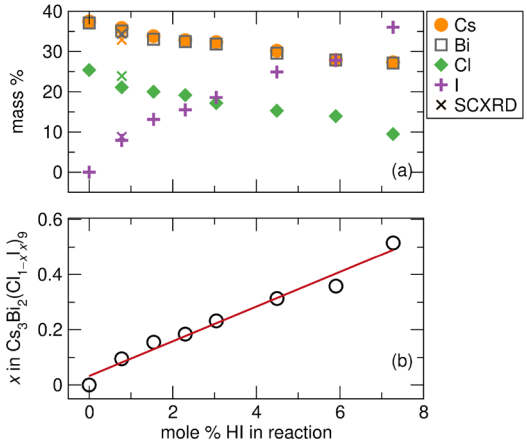

Figure 2. (a) Compositions of the title compounds as determined by XRF as a function of the percentage of HI in the reaction mixture. For the solid solution compound $Cs_3Bi_2Cl_{8.16}I_{0.84}$, the composition obtained from SCXRD refinement is indicated in the appropriate location. (b) I/Cl mass ratios from XRF converted to values of x in $Cs_3Bi_2(Cl_{1-x}I_x)_9$.

Figure 3 displays the evolution of PXRD patterns of the different compounds in the solid solution that crystallize in the 2D vacancy-ordered perovskite structure in space group $P\bar{3}m1$. The overlaid Rietveld fits suggest that all of the samples are single phase within the detection limits established by laboratory X-ray diffraction data. In the case of the end-member compounds, PXRD patterns for $Cs_3Bi_2Cl_9$ and

https://dx.doi.org/10.1021/acs.inorgchem.9b03415
Inorg. Chem. 2020, 59, 3387−3393

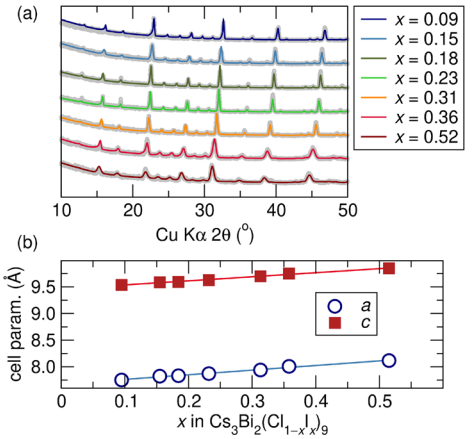

Figure 3. (a) Evolution of X-ray diffraction patterns of the compounds $Cs_3Bi_2(Cl_{1-x}I_x)_9$ with the single-phase Rietveld fits to the 2D vacancy-ordered perovskite structure overlaid. Rietveld analysis confirms the absence of extraneous peaks that would suggest a secondary phase. (b) Evolution of the cell parameters with x of $Cs_3Bi_2(Cl_{1-x}I_x)_9$.

$Cs_3Bi_2I_9$ (not displayed) matched those of previously reported structures for α-$Cs_3Bi_2Cl_9$ and bulk $Cs_3Bi_2I_9$. In addition to a shift to lower 2θ values with increasing iodine content, the peaks also exhibit broadening with increasing amounts of iodine, as shown in Figure 3. This broadening is attributed to the decreasing size of the crystallites as the amount of iodine in the sample increases.

Diffuse-reflectance spectra transformed using the Kubelka–Munk method into absorbance for each compound are shown in Figure 4. As expected from the appearance of the compounds, which range from yellow to orange, the absorption edge shifts to lower energies with increasing I occupancy. Additionally, the absorbance peak widens with increasing iodine. From the absorbance data, the absorbance edge for each compound was calculated and is presented as a function of the composition in Figure 4b. A large decrease in

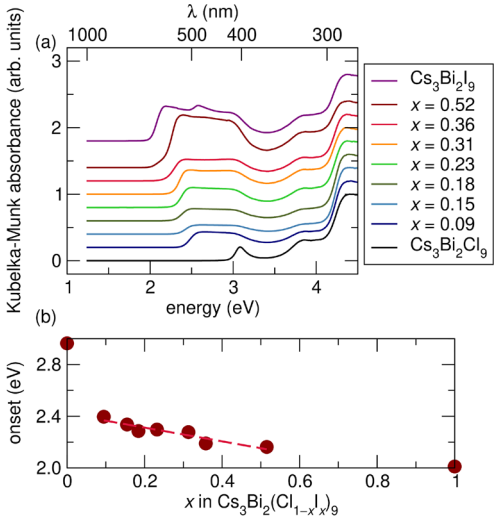

Figure 4. (a) Kubelka–Munk-transformed optical absorption data on powders of $Cs_3Bi_2(Cl_{1-x}I_x)_9$. (b) Absorption onset as a function of x. The inset displays a photograph of the as-prepared samples of $Cs_3Bi_2(Cl_{1-x}I_x)_9$ in their reactant solution, with x increasing from 0.09 to 0.52 from left to right.

the energy of the first absorption edge is noted immediately upon iodine incorporation, corresponding to a change from the 1D structure to the 2D structure. As more iodine is incorporated into the lattice, the energy of the absorption edge decreases nearly linearly with the increasing I occupancy.

DFT-based calculations were carried out in order to gain a better understanding of the electronic structures of these new compounds, including the relative roles of structural connectivity and iodine substitution in the measured band gaps. Figure 5 presents the calculated band gaps of compounds

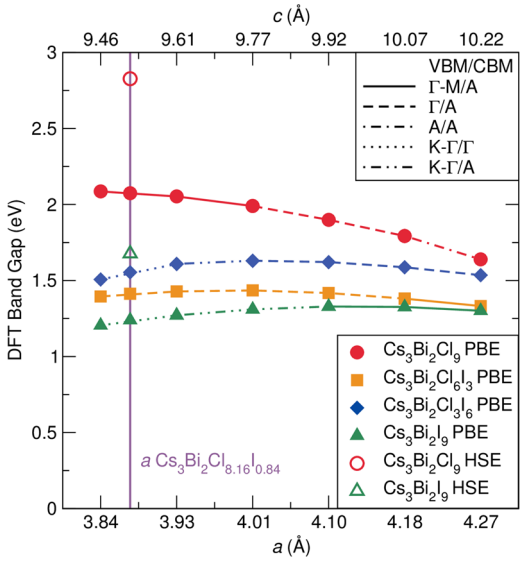

Figure 5. DFT band gaps of compounds in the vacancy-ordered 2D perovskite structure in space group $P\bar{3}m1$. We compare simulations of compounds $Cs_3Bi_2Cl_9$, $Cs_3Bi_2Cl_6I_3$, $Cs_3Bi_2Cl_3I_6$, and $Cs_3Bi_2I_9$ with varying iodine filling and lattice parameters. In addition, we repeated all of the calculations using the lattice parameters of $Cs_3Bi_2Cl_{8.16}I_{0.84}$ determined by SCXRD (Note: the c/a ratio for $Cs_3Bi_2Cl_{8.16}I_{0.84}$ is slightly different from that determined by powder Rietveld refinement, so the c axis is not valid for these data points; the adjustment is very minor, however.) All simulations incorporated spin–orbit coupling.

with vacancy-ordered perovskite structures. This includes hypothetical compounds with compositions of $Cs_3Bi_2Cl_9$, $Cs_3Bi_2I_9$, and $Cs_3Bi_2Cl_3I_6$, in which the I atom sits on the 6i capping Wyckoff site and the Cl atom sits on the 3e site, and $Cs_3Bi_2Cl_6I_3$, in which Cl and I occupation is reversed to the 6i and 3e sites, respectively. The treatment of these four structures provides a qualitative understanding of the role of I site occupation without breaking the space group symmetry and needing to consider more complex supercell calculations. In addition to stoichiometric changes, there is significant lattice expansion with increased iodine concentration. In order to account for this effect, we have repeated calculations for all four structures at lattice parameters corresponding to 0%, 20%, 40%, 60%, 80%, and 100% iodine substitution based on the linear lattice parameter trends of the powder Rietveld fits (Figure 3) as well as the lattice parameters of single-crystal $Cs_3Bi_2Cl_{8.16}I_{0.84}$.

Transitions of the valence band maximum (VBM) and conduction band minimum (CBM) in Figure 5 are displayed using dashed lines. We find that, across this solid solution, as in other perovskite systems with relatively flat conduction bands,[37] a great number of direct and indirect transitions can

https://dx.doi.org/10.1021/acs.inorgchem.9b03415
Inorg. Chem. 2020, 59, 3387–3393

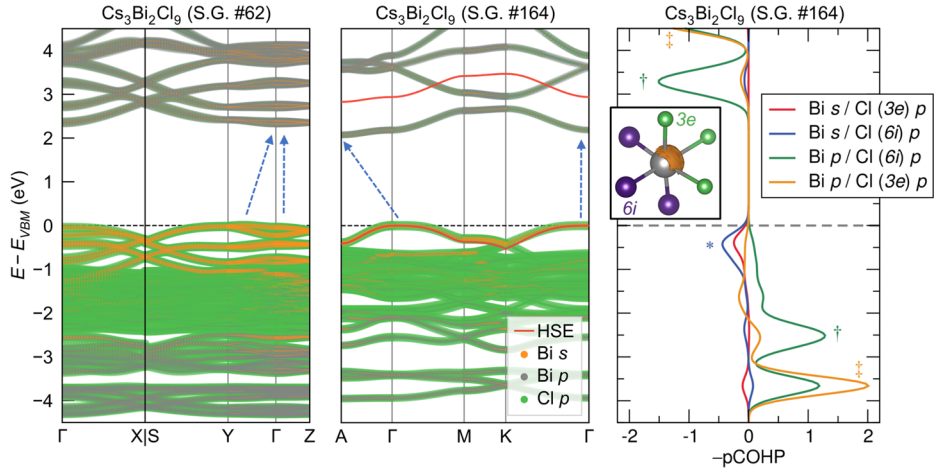

Figure 6. Calculated band structures of $Cs_3Bi_2Cl_9$ in the 1D chain structure [*Pnma* (No. 62)] of $Cs_3Bi_2Cl_9$ and 2D vacancy-ordered perovskite structure [$P\bar{3}m1$ (No. 164)] of $Cs_3Bi_2Cl_{8.16}I_{0.84}$. The size of the dots represents the relative magnitude of orbital projections. Blue arrows indicate the smallest direct and indirect band gaps (Γ/Γ;Γ−*Y*/Γ for the *Pnma* structure and Γ/Γ;Γ−*M*/*A* for the $P\bar{3}m1$ structure). The HSE conduction and valence bands are provided for reference on the space group No. 164 band structure. The third panel shows bond-projected COHP pairs for Bi−Cl orbital bonding with Cl atoms on the 3e and 6i octahedral sites. The inset shows the electron localization function on the Bi atom at a contour of 0.57 electron in relation to the 3e and 6i sites. Annotations indicate (*) Bi s−Cl p antibonding contribution at the VBM, (†) Bi p−Cl(6i) p bonding and antibonding states that contribute to the CBM, and (‡) Bi p−Cl(3e) p bonding and antibonding states that contribute to neither the CBM nor VBM.

be favored based on subtle changes in bonding. Second, the fact that both $Cs_3Bi_2Cl_9$ and $Cs_3Bi_2I_9$ in the vacancy-ordered perovskite structure adopt a Γ−*M*/*A* gap at their preferred lattice parameters suggests that the dominant transitions in the real material should be close to Γ−*M*/*A*.

Upon comparison with the calculated band gap (PBE) for the 1D chain (*Pnma*) of the $Cs_3Bi_2Cl_9$ structure of 2.32 eV (Figure 6), the band gap of $Cs_3Bi_2Cl_9$ in the hypothetical 0% Cl $P\bar{3}m1$ structure is 2.09 eV, which is smaller, but not significantly so. A comparison of the large optical absorption onset energy decreases of the first two data points of Figure 4b (≈0.5 eV) suggests that structural transformation to the 2D connectivity alone is not sufficient to recreate the band-gap trend. The lattice parameter trend alone also appears insufficient to explain the large reduction in the experimental band gap. While the band gap of $Cs_3Bi_2Cl_9$ decreases by about 0.3 eV upon compression to the $Cs_3Bi_2I_9$ structure, the trend is reversed for any of the structures with iodine. The full iodine structure has a much smaller band gap than the full Cl structure, and the magnitude of this reduction is consistent with the large drop seen in the experiment. This is not surprising because of the relatively large size of iodine orbitals compared to chlorine orbitals and the expectation that there will therefore be larger band dispersion in the iodine compound. The HSE band gaps, which are expected to quantitatively match the measured values more closely than the PBE values, further confirm this intuition. The HSE band gap of the full chlorine compound is quite close to that of $Cs_3Bi_2Cl_9$ measured in the experiment, and the 2.8−1.7 eV band-gap range between chlorine and iodine compounds is roughly consistent with the range seen in the experiment, albeit downshifted by about 0.2 eV from the values of Figure 4b.

A more subtle point is that the band gap of $Cs_3Bi_2Cl_6I_3$ is systematically lower than that of $Cs_3Bi_2Cl_3I_6$. This may seem surprising at first because the latter structure has double the concentration of iodine. This is due to the different bond distances and bond strengths for the 6i and 3e site occupancies. The value of the integrated crystal orbital Hamilton population (ICOHP) has been found to form an effective computational proxy for bond strength in a wide variety of systems. The more negative the ICOHP, the stronger the bonding. Larger ICOHPs evidence stronger bonding in the full iodine structures: −3.4 and −2.1 eV for Bi−I bonding in $Cs_3Bi_2I_9$ on 6i and 3e sites, respectively, while for Bi−Cl bonding in $Cs_3Bi_2I_9$ on the same sites, these values are −2.5 and −1.5 eV (here, we consider the ICOHP in the single-crystal structure of $Cs_3Bi_2Cl_{8.16}I_{0.84}$). Moreover, the bonding strength of iodine on the 6i capping site is much greater than that on the 3e site or chlorine on either site; this may explain the strong preference for iodine occupation on the 6i site. The bonding asymmetry is more broadly reflective of asymmetry in the electron distribution near the Bi atom. The inset of Figure 6 shows the electron localization function of the Bi atom in relation to the octahedral bonding, demonstrating a stereochemically active lone pair that points away from the 6i sites and toward the 3e sites.

Figure 6 shows selected portions of the orbital-projected band structures of $Cs_3Bi_2Cl_9$ in the 2D vacancy-ordered perovskite structure ($P\bar{3}m1$) and the structure with 1D chains (*Pnma*). As expected, the 2D-bonding connectivity structure can be seen to have larger band dispersions in both the conduction and valence bands than the 1D-connectivity *Pnma* structure. As in many other perovskite systems, electron filling of the Cl/I p orbitals and the loss of electrons by Bi p yields a band structure with dominant Cl/I p contributions in the valence band and dominant Bi p in the conduction band. A large Bi s contribution at the top of the valence band arises due to Bi s−Cl p antibonding interactions. The third panel of Figure 6 presents the unintegrated partial COHP of Bi−Cl bonding interactions in the 2D $P\bar{3}m1$ structure. Atoms on both the 6i and 3e sites contribute to the Bi s−Cl p antibonding interactions (*) that push the VBM upward in energy, whereas only atoms on the 6i site contribute to the Bi p−Cl p antibonding interaction (†) that pushes the CBM upward in energy. This explains why the band gap of $Cs_3Bi_2Cl_6I_3$ is lower than that of $Cs_3Bi_2Cl_3I_6$. While placing iodine on either site

https://dx.doi.org/10.1021/acs.inorgchem.9b03415
Inorg. Chem. 2020, 59, 3387−3393

increases the bonding strength and band dispersion, ultimately closing the band gap, placing iodine on the nonpreferred 3e site raises the energy of the Bi s−Cl p antibonding states in the valence band without also raising the energy of the antibonding Bi p−Cl p states in the conduction band, closing the band gap much more rapidly.

Overall, the computational results suggest that, in addition to the increased 2D bonding connectivity in the vacancy-ordered perovskite structures, the effect of iodine incorporation on local bonding is essential to explaining the sharp reduction in the band gap seen in the experiment. Bonding asymmetry due to the stereochemically active lone pair on the Bi atom is likely one reason for the preference for iodine occupation on the capping sites.

CONCLUSION

We have shown that even small iodine incorporation (small x) in the solid solution $Cs_3Bi_2(Cl_{1-x}I_x)_9$ switches the structure to the vacancy-ordered perovskite type in the trigonal space group $P\bar{3}m1$. Associated with this substitution are dramatic changes in the optical properties, which can be further tuned with increasing iodine incorporation. DFT-based electronic structure calculations point to the importance of the electronic changes induced by the orbital states of I over the changes in the structural dimensionality as dominating the changes in the optical absorption properties. They also point to the potential origin of the site-preference tendency of I^- that results in the structure being switched from 1D to perovskite-derived 2D upon I^- incorporation.

ASSOCIATED CONTENT

Supporting Information

The Supporting Information is available free of charge at https://pubs.acs.org/doi/10.1021/acs.inorgchem.9b03415.

Optical microscopic images (Figure S1), additional crystallographic data (Tables S1−S6), Rietveld fit depictions for all of the samples (Figures S2−S8), and computational data (Tables S7−S10) (PDF)

Accession Codes

CCDC 1967123 and 1967124 contain the supplementary crystallographic data for this paper. These data can be obtained free of charge via www.ccdc.cam.ac.uk/data_request/cif, or by emailing data_request@ccdc.cam.ac.uk, or by contacting The Cambridge Crystallographic Data Centre, 12 Union Road, Cambridge CB2 1EZ, UK; fax: +44 1223 336033.

AUTHOR INFORMATION

Corresponding Author

Lingling Mao − *Materials Research Laboratory, University of California at Santa Barbara (UCSB), Santa Barbara, California 93106, United States;* orcid.org/0000-0003-3166-8559; Email: linglingmao@ucsb.edu

Authors

Emily E. Morgan − *Materials Research Laboratory and Materials Department, University of California at Santa Barbara (UCSB), Santa Barbara, California 93106, United States*

Samuel M. L. Teicher − *Materials Research Laboratory and Materials Department, University of California at Santa Barbara (UCSB), Santa Barbara, California 93106, United States;* orcid.org/0000-0002-5922-4258

Guang Wu − *Department of Chemistry and Biochemistry, University of California at Santa Barbara (UCSB), Santa Barbara, California 93106, United States*

Ram Seshadri − *Materials Research Laboratory, Materials Department, and Department of Chemistry and Biochemistry, University of California at Santa Barbara (UCSB), Santa Barbara, California 93106, United States;* orcid.org/0000-0001-5858-4027

Complete contact information is available at: https://pubs.acs.org/10.1021/acs.inorgchem.9b03415

Notes

The authors declare no competing financial interest.

ACKNOWLEDGMENTS

This work was supported by the U.S. Department of Energy, Office of Science, Basic Energy Sciences, under Award DE-SC-0012541. Use of the Shared Experimental Facilities of the Materials Research Science and Engineering Center (MRSEC) at UCSB (NSF Grant DMR 1720256) is gratefully acknowledged. The UCSB MRSEC is a member of the NSF-supported Materials Research Facilities Network (www.mrfn.org). We additionally acknowledge support from the Center for Scientific Computing at UCSB, supported by NSF Grants CNS-1725797 and DMR-1720256. S.M.L.T. has been supported by the National Science Foundation Graduate Research Fellowship Program under Grant DGE-1650114. Any opinions, findings, and conclusions or recommendations expressed in this material are those of the authors and do not necessarily reflect the views of the National Science Foundation (NSF). The authors thank Prof. Constantinos Stoumpos for helpful discussion on structural analysis.

REFERENCES

(1) Snaith, H. J. Present Status and Future Prospects of Perovskite Photovoltaics. *Nat. Mater.* **2018**, *17*, 372−376.

(2) National Renewable Energy Laboratory. Best Research-Cell Efficiency Chart, https://www.nrel.gov/pv/cell-efficiency.html.

(3) Saparov, B.; Mitzi, D. B. Organic-Inorganic Perovskites: Structural Versatility for Functional Materials Design. *Chem. Rev.* **2016**, *116*, 4558−4596.

(4) Wang, H.; Bian, H.; Jin, Z.; Zhang, H.; Liang, L.; Wen, J.; Wang, Q.; Ding, L.; Liu, S. F. Cesium Lead Mixed-Halide Perovskites for Low Energy Loss Solar Cells with Efficiency Beyond 17%. *Chem. Mater.* **2019**, *31*, 6231.

(5) Fabini, D. Quantifying the Potential for Lead Pollution from Halide Perovskite Photovoltaics. *J. Phys. Chem. Lett.* **2015**, *6*, 3546−3548.

(6) Babayigit, A.; Ethirajan, A.; Muller, M.; Conings, B. Toxicity of Organometal Halide Perovskite Solar Cells. *Nat. Mater.* **2016**, *15*, 247−251.

(7) Shi, Z.; Guo, J.; Chen, Y.; Li, Q.; Pan, Y.; Zhang, H.; Xia, Y.; Huang, W. Lead-Free Organic−Inorganic Hybrid Perovskites for Photovoltaic Applications: Recent Advances and Perspectives. *Adv. Mater.* **2017**, *29*, 1605005.

(8) Park, B.-W.; Philippe, B.; Zhang, X.; Rensmo, H.; Boschloo, G.; Johansson, E. M. Bismuth Based Hybrid Perovskites $A_3Bi_2I_9$ (*A*: Methylammonium or Cesium) for Solar Cell Application. *Adv. Mater.* **2015**, *27*, 6806−6813.

(9) Abulikemu, M.; Ould-Chikh, S.; Miao, X.; Alarousu, E.; Murali, B.; Ngongang Ndjawa, G. O.; Barbé, J.; El Labban, A.; Amassian, A.; Del Gobbo, S. Optoelectronic and Photovoltaic Properties of the Air-Stable Organohalide Semiconductor $(CH_3NH_3)_3Bi_2I_9$. *J. Mater. Chem. A* **2016**, *4*, 12504−12515.

(10) Creutz, S. E.; Liu, H.; Kaiser, M. E.; Li, X.; Gamelin, D. R. Structural Diversity in Cesium-Bismuth-Halide Nanocrystals. *Chem. Mater.* **2019**, *31*, 4685−4697.
(11) Lehner, A. J.; Wang, H.; Fabini, D. H.; Liman, C. D.; Hébert, C.-A.; Perry, E. E.; Wang, M.; Bazan, G. C.; Chabinyc, M. L.; Seshadri, R. Electronic Structure and Photovoltaic Application of BiI_3. *Appl. Phys. Lett.* **2015**, *107*, 131109.
(12) Lehner, A. J.; Fabini, D. H.; Evans, H. A.; Hébert, C.-A.; Smock, S. R.; Hu, J.; Wang, H.; Zwanziger, J. W.; Chabinyc, M. L.; Seshadri, R. Crystal and Electronic Structures of Complex Bismuth Iodides $A_3Bi_2I_9$ (A = K, Rb, Cs) Related to Perovskite: Aiding the Rational Design of Photovoltaics. *Chem. Mater.* **2015**, *27*, 7137−7148.
(13) Lou, Y.; Fang, M.; Chen, J.; Zhao, Y. Formation of Highly Luminescent Cesium Bismuth Halide Perovskite Quantum Dots Tuned by Anion Exchange. *Chem. Commun.* **2018**, *54*, 3779−3782.
(14) Leng, M.; et al. All-Inorganic Bismuth-Based Perovskite Quantum Dots with Bright Blue Photoluminescence and Excellent Stability. *Adv. Funct. Mater.* **2018**, *28*, 1704446.
(15) Jain, S. M.; Phuyal, D.; Davies, M. L.; Li, M.; Philippe, B.; De Castro, C.; Qiu, Z.; Kim, J.; Watson, T.; Tsoi, W. C.; Karis, O.; Rensmo, H.; Boschloo, G.; Edvinsson, T.; Durrant, J. R. An Effective Approach of Vapour Assisted Morphological Tailoring for Reducing Metal Defect Sites in Lead-Free, $(CH_3NH_3)_3Bi_2I_9$ Bismuth-Based Perovskite Solar Cells for Improved Performance and Long-Term Stability. *Nano Energy* **2018**, *49*, 614−624.
(16) Xiao, Z.; Meng, W.; Wang, J.; Mitzi, D. B.; Yan, Y. Searching for Promising New Perovskite-Based Photovoltaic Absorbers: the Importance of Electronic Dimensionality. *Mater. Horiz.* **2017**, *4*, 206−216.
(17) McCall, K. M.; Stoumpos, C. C.; Kontsevoi, O. Y.; Alexander, G. C.; Wessels, B. W.; Kanatzidis, M. G. From 0D $Cs_3Bi_2I_9$ to 2D $Cs_3Bi_2I_6Cl_3$: Dimensional Expansion Induces a Direct Band Gap but Enhances Electron−Phonon Coupling. *Chem. Mater.* **2019**, *31*, 2644−2650.
(18) Coelho, A. A. TOPAS and TOPAS-Academic: An Optimization Program Integrating Computer Algebra and Crystallographic Objects Written in C++. *J. Appl. Crystallogr.* **2018**, *51*, 210−218.
(19) Dolomanov, O. V.; Bourhis, L. J.; Gildea, R. J.; Howard, J. A. K.; Puschmann, H. OLEX2: A Complete Structure Solution, Refinement and Analysis Program. *J. Appl. Crystallogr.* **2009**, *42*, 339−341.
(20) Momma, K.; Izumi, F. VESTA 3 for Three-Dimensional Visualization of Crystal, Volumetric and Morphology Data. *J. Appl. Crystallogr.* **2011**, *44*, 1272−1276.
(21) Kubelka, P. Ein Beitrag zur Optik der Farbanstriche. *Z. Phys.* **1931**, *12*, 593−601.
(22) Kresse, G.; Hafner, J. Ab Initio Molecular-Dynamics Simulation of the Liquid-Metal−Amorphous-Semiconductor Transition in Germanium. *Phys. Rev. B: Condens. Matter Mater. Phys.* **1994**, *49*, 14251.
(23) Kresse, G.; Furthmüller, J. Efficient Iterative Schemes for Ab Initio Total-Energy Calculations Using a Plane-Wave Basis Set. *Phys. Rev. B: Condens. Matter Mater. Phys.* **1996**, *54*, 11169.
(24) Kresse, G.; Furthmüller, J. Efficiency of ab-initio Total Energy Calculations for Metals and Semiconductors Using a Plane-Wave Basis Set. *Comput. Mater. Sci.* **1996**, *6*, 15.
(25) Perdew, J. P.; Burke, K.; Ernzerhof, M. Generalized Gradient Approximation Made Simple. *Phys. Rev. Lett.* **1996**, *77*, 3865.
(26) Heyd, J.; Scuseria, G. E.; Ernzerhof, M. Erratum: "Hybrid functionals based on a screened Coulomb potential" [J. Chem. Phys. 118, 8207 (2003)]. *J. Chem. Phys.* **2006**, *124*, 219906.
(27) Blöchl, P. E. Projector Augmented-Wave Method. *Phys. Rev. B: Condens. Matter Mater. Phys.* **1994**, *50*, 17953.
(28) Kresse, G.; Joubert, D. From Ultrasoft Pseudopotentials to the Projector Augmented-Wave Method. *Phys. Rev. B: Condens. Matter Mater. Phys.* **1999**, *59*, 1758.
(29) Dronskowski, R.; Bloechl, P. E. Crystal Orbital Hamilton populations (COHP): Energy-Resolved Visualization of Chemical Bonding in Solids Based on Density-Functional Calculations. *J. Phys. Chem.* **1993**, *97*, 8617.
(30) Deringer, V. L.; Tchougréeff, A. L.; Dronskowski, R. Crystal Orbital Hamilton Population (COHP) Analysis As Projected from Plane-Wave Basis Sets. *J. Phys. Chem. A* **2011**, *115*, 5461.
(31) Maintz, S.; Deringer, V. L.; Tchougréeff, A. L.; Dronskowski, R. Analytic Projection from Plane-Wave and PAW Wavefunctions and Application to Chemical-Bonding Analysis in Solids. *J. Comput. Chem.* **2013**, *34*, 2557.
(32) Maintz, S.; Deringer, V. L.; Tchougréeff, A. L.; Dronskowski, R. LOBSTER: A Tool to Extract Chemical Bonding from Plane-Wave Based DFT. *J. Comput. Chem.* **2016**, *37*, 1030.
(33) Meyer, G.; Schönemund, A. Zur Kenntnis der Hochtemperatur-Phasenumwandlug bei $Cs_3Bi_2Cl_9$. *Z. Anorg. Allg. Chem.* **1980**, *468*, 185−192.
(34) Arakcheeva, A.; Novikova, M.; Zaitsev, A.; Lubman, G. Perovskite-like Modification of $Cs_3Sb_2I_9$ as a Member of the OD family $A_3B_2X_9$. *J. Struct. Chem.* **1999**, *40*, 572−579.
(35) Dornberger-Schiff, K.; Grell-Niemann, H. On the Theory of Order−Disorder (OD) Structures. *Acta Crystallogr.* **1961**, *14*, 167−177.
(36) Benachenhou, F.; Mairesse, G.; Nowogrocki, G.; Thomas, D. Structural Studies of Cs−K−Bi Mixed Chlorides Relation to the Crystal Structures of A_2BMX_6, A_3MX_6, and A_2MX_6. *J. Solid State Chem.* **1986**, *65*, 13−26.
(37) Mao, L.; Teicher, S. M. L.; Stoumpos, C. C.; Kennard, R. M.; DeCrescent, R. A.; Wu, G.; Schuller, J. A.; Chabinyc, M. L.; Cheetham, A. K.; Seshadri, R. Chemical and Structural Diversity of Hybrid Layered Double Perovskite Halides. *J. Am. Chem. Soc.* **2019**, *141*, 19099.

https://dx.doi.org/10.1021/acs.inorgchem.9b03415
Inorg. Chem. 2020, 59, 3387−3393